ChemCatChem

Research Article
doi.org/10.1002/cctc.202400450

Chemistry Europe
European Chemical Societies Publishing

www.chemcatchem.org

Hydrogen Evolving Mono-Nuclear Manganese Complexes with Carefully Positioned Pyridine Base Ligands

Fatimah Ali Hussein,[a] Meenakshi Joshi,[b] Sandeep Kaur-Ghumaan,*[a] and Matthias Stein*[b]

Dedicated to Prof. Wolfgang Lubitz on the occasion of his 75th birthday.

Enormous efforts have been made by the scientific community in the development of bio-mimetic/bio-inspired hydrogen-evolving complexes as catalysts for an alternative hydrogen energy carrier and renewable energy sources. In this regard, new bio-inspired mono-nuclear Mn(I) carbonyl model complexes *fac*-[(Mn(CO)$_3$(κ^2-SN$_2$C$_7$H$_5$)(κ^1-PPh$_2$Py))] **1** and *fac*-[(Mn-(CO)$_3$(κ^2-S$_2$NC$_7$H$_4$)(κ^1-PPh$_2$Py))] **2** with 2-mercaptobenzimidazole (N,N) and 2-mercaptobenzothiazole (S,N) ligands and a N-based phosphine ligand (PPh$_2$Py) have been synthesized, spectroscopically characterized and evaluated as electro-catalysts for hydrogen generation. In contrast to related mono-nuclear (N,N/S,N)–Mn–PPh$_3$ complexes, the newly introduced pyridine nitrogen atom of the PPh$_2$Py ligand placed in an axial position in the second coordination sphere of the Mn(I) complexes, provides a first site for protonation and enables a fast intra-molecular proton transfer to the central metal atom with a weaker acid. Theoretical DFT calculations enable a detailed picture of catalytic pathways, assign redox transitions and structural changes. Both the molecular complexes were tested as electro-catalysts for hydrogen generation in CH$_3$CN. Complexes **1** and **2** effectively catalyzed the electrochemical proton reduction with the weaker acetic acid as the proton source and displayed a turnover frequency (*TOF*/s^{-1}; overpotential, η/V) of 610; 1.02 and 615; 1.12, respectively. [Correction added on 25 July 2024, after first online publication: Preceding sentence was updated.] The computer-aided design of dedicated proton transfer pathways from second coordination sphere ligands is thus able to allow a hydrogen evolution reactivity with a weaker acid (acetic acid).

Introduction

On the route to a net zero-carbon emission scenario, molecular hydrogen (H$_2$) is one of the most-promising energy carriers.[1–3] The design and development of novel molecular catalytic systems for the hydrogen evolution reaction (HER) have received significant attention during the last decade. Mono-nuclear catalysts, however, are so far less explored but have the advantage of a more facile synthesis and give a higher density of catalytic sites. Those previously reported contain, among others, Fe,[4,5] Co[6–9] and Ni[9,10,11] as transition metals. Recently, also metal porphyrins containing Ga[12] and Co[13,14] have been shown to be active and robust electrocatalysts for HER.

The hydrogen-evolving enzyme [FeFe] hydrogenase contains an aza-bis(dithiolate) (adt) ligand[15,16] that acts as an efficient proton relay and first site of protonation (see Figure 1). Only a single carefully positioned pendant amine is required to serve this function. The presence of a pendant amine ligand in

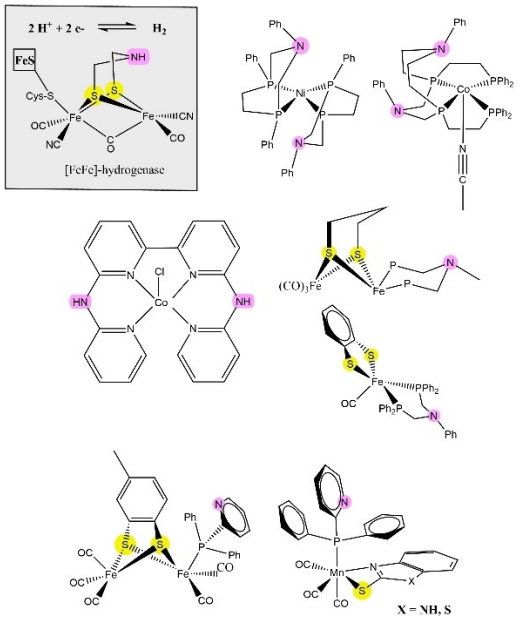

Figure 1. Selected examples of carefully positioned proton relays in hydrogen-evolving catalysts such as mono-nuclear Ni,[9] Co,[25,26] di-nuclear[27–29] and mono-nuclear Fe[23] complexes and this work.

[a] F. A. Hussein, Prof. S. Kaur-Ghumaan
Department of Chemistry, University of Delhi (North Campus), Delhi 110007, India
E-mail: skaur@chemistry.du.ac.in

[b] Dr. M. Joshi, Prof. M. Stein
Molecular Simulations and Design Group
Max Planck Institute for Dynamics of Complex Technical Systems,
Sandtorstrasse 1, 39106 Magdeburg, Germany
E-mail: matthias.stein@mpi-magdeburg.mpg.de

Supporting information for this article is available on the WWW under https://doi.org/10.1002/cctc.202400450

the second coordination sphere facilitates protonation and formation of a metal-hydride species by fine-tuning the pK_a and acting as a proton relay shuttle.[17] An overview of intra-molecular proton transfer regarding the engineering of enzymatic and bio-inspired systems can be found in refs.[18,19] In addition to pioneering concepts of designing intra-molecular proton relays (see below), recent examples in hydrogen-evolving catalysts include, among others, rhodium dimers,[20] cobalt(III),[21] and Ni(II).[22] However, the flexibility of tertiary amines affords a large number of accessible conformers with different orientations of the nitrogen's lone pair orbital.[23]

Figure 1 shows selected examples for the introduction of nitrogen-containing ligands into the second coordination sphere of HER catalysts. In particular, the intramolecular proton transfer from the protonated ligand to the metal is critical for an efficient electrochemical proton reduction.[9] In a bi-metallic system, the position of the nitrogen ligand can even control the site of reactivity.[24]

Manganese is an exquisite catalyst for oxygen reduction and evolution.[30] Like Fe, Mn is a cheap, non-precious and highly abundant metal and Mn(I) complexes have recently been used also as selective CO_2 reducing catalysts.[31,32] However, its performance in catalysing HER has not been fully explored until now.[33,34] The design of an artificial, non-native Mn^{I} catalyst with the abundant bio-inorganic Fe^{II} suggested that also Mn^{I}-based complexes may be suitable HER catalysts.[35]

Here, we report the synthesis of mono-nuclear proton-reducing manganese catalysts[36] with a pyridine ligand positioned in axial position to the transition metal (see Figure 2). In pyridine, the sp^2-hybridized nitrogen atom is not part of the aromatic π-electron system and thus accessible to protonation. The equatorial ligands κ^2-$S_2NC_7H_4$ and κ^2-$SN_2C_7H_5$ and three CO ligands complete the octahedral coordination sphere.

Results and Discussion

Synthesis and Characterization

Mononuclear Mn(I) carbonyl complexes, *fac*-[(Mn(CO)$_3$(κ^2-$SN_2C_7H_5$)(κ^1-PPh_2Py))] **1** and *fac*-[(Mn(CO)$_3$(κ^2-$S_2NC_7H_4$)(κ^1-PPh_2Py))] **2**, were synthesized under aerobic conditions from the reaction of dinuclear Mn complexes [$Mn_2(CO)_6$(μ-$SN_2C_7H_5$)$_2$] **A** and [$Mn_2(CO)_6$(μ-$S_2NC_7H_4$)$_2$] **B** with diphenyl-2-pyridyl phosphine (PPh_2Py) in dichloromethane for 72 h at room temperature (see Scheme 1). Complexes **1** and **2** were obtained as air-stable yellow solids and were characterized using different spectroscopic techniques such as FTIR, ^{1}H and ^{31}P NMR and Mass Spectrometry (MS) (see Supplementary Figures S1–S9, ESI). The ^{1}H NMR spectra of complexes **1** and **2** displayed resonance peaks in the range of 6.84–8.71 and 7.06–8.41 ppm, respectively (Figures S1–S2). These peaks are associated with the aromatic protons of the ligands attached to the Mn atom. The ^{31}P{^{1}H}[23] NMR spectra displayed singlets at 56.5 (**1**), 57.4 (**2**) (Figures S3–S4). The PPh_2Py ligand on the other hand, displayed a singlet at −3.44 ppm in the ^{31}P{^{1}H} NMR spectrum thus, confirming the coordination between P and Mn (see Figure S5). [Correction added on 25 July 2024, after first online publication: {1H} was corrected to {^{1}H} in the preceding sentence.] The FTIR spectra of complexes **1** and **2** recorded in dichloromethane showed absorption bands between 2022 and 1906 cm^{-1} (Figure S6), indicating that all carbonyl ligands in the complexes are terminal in nature which are identical to the related complexes reported earlier.[36,37] Complexes **1** and **2** exhibited molecular masses m/z at 552.03 and 568.99 corresponding to [**1** + H]$^+$ and [**2** + H]$^+$, respectively (Figures S7–S8). The UV-Vis measurements for complexes **1** and **2** recorded in CH_3CN showed absorption bands in the range 300–327 nm, which could be assigned to π–π* and n–π* transitions (Figure S9). Complex **2** showed bands at higher wavelength in comparison to complex **1**, which could be assigned to n-π* transitions and a lower HOMO-LUMO gap in **2**.

Single crystals could be obtained for complexes **1** and **2** and were analyzed by single-crystal X-ray diffraction. The crystallographic parameters, selected bond lengths and bond angles of complexes **1** and **2** are reported in Tables S1–S3 in the Supporting Information (see ESI). X-ray structure analyses confirmed the equatorial chelation by 2-mercaptobenzimidazole/2-mercaptobenzothiazole through N1 and S1, the axial PPh_2Py and three carbonyl groups completing a distorted octahedral geometry (see Figure 3).

Figure 2. Modification and introduction of an axial pyridine ligand in the second coordination sphere of a mono-nuclear manganese hydrogen evolving complex.

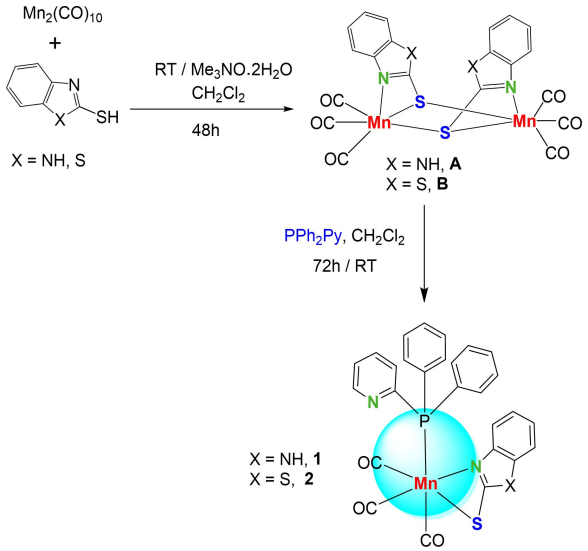

Scheme 1. Synthetic scheme for complexes *fac*-[(Mn(CO)$_3$(κ^2-$SN_2C_7H_5$)(κ^1-PPh_2Py))] **1** and *fac*-[(Mn(CO)$_3$(κ^2-$S_2NC_7H_4$)(κ^1-PPh_2Py))] **2**.

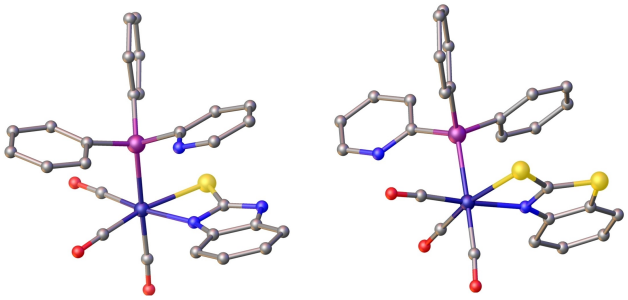

Figure 3. X-ray single-crystal structures for *fac*-[(Mn(CO)$_3$(κ^2-SN$_2$C$_7$H$_5$)(κ^1-PPh$_2$Py))] **1** and *fac*-[(Mn(CO)$_3$(κ^2-S$_2$NC$_7$H$_4$)(κ^1-PPh$_2$Py))] **2**. Thermal ellipsoids correspond to 50% probability. Hydrogen atoms have been omitted for clarity. Two molecules of **1** were present in the unit cell.

Redox Activity of Mono-Nuclear Mn(I) Complexes

Cyclic voltammetry (CV) measurements for complexes **1** and **2** were performed in organic media (CH_3CN) with a glassy carbon working electrode using 0.1 M tetrabutylammonium hexafluorophosphate [N(n-Bu$_4$)][PF$_6$] as the supporting electrolyte. The CVs of the complexes for oxidation are shown in Figure S10. Scan rate linear dependence measurements demonstrate that all the redox processes are diffusion-controlled. Complexes **1** and **2** show irreversible reduction peaks at −1.97/−2.29 V and −1.89/−2.04 V *vs.* Fc/Fc$^+$, respectively (see Figure 4). Assignment of CV spectral peaks to redox transitions is difficult and performed on the basis of DFT calculations. According to the computational results, these correspond to a two-electron reduction and the second one-electron reduction events (see below). The Mn^{I} → Mn^{0} redox process cannot be resolved in experimental spectra.

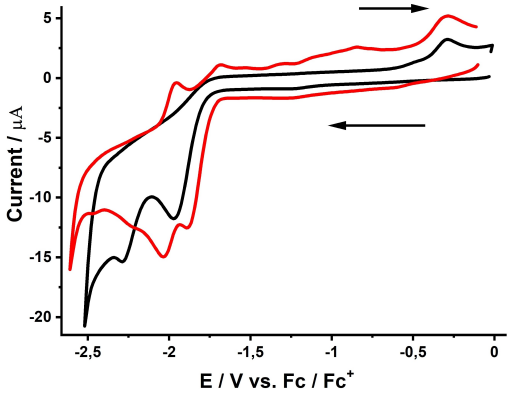

Figure 4. Cyclic voltammograms for reduction of complexes **1** (—) and **2** (—) (1 mM) in CH_3CN at a scan rate of 0.1 Vs^{-1}.

Table 1. Experimental and calculated redox transitions in eV relative to Fc$^+$/Fc.

	Experimental		Calc. MnP(Ph)$_2$Py
	Mn–P(Ph)$_3$	Mn–P(Ph)$_2$Py	BP86/PBE0/r2scan
1 (NH)			
1/1$^-$	n.r.	n.r.	−1.82/−1.81/−1.76
1$^-$**/1**$^{2-}$	−2.36	−2.29	−2.15/−2.38/−2.14
1/1^{2-}	−2.06	−1.97	−1.99/−2.10/−1.95
2 (S)			
2/2$^-$	n.r.	n.r.	−1.83/−1.86/−1.78
2$^-$**/2**$^{2-}$	−2.07	−2.04	−2.16/−2.37/−2.12
2/2^{2-}	−1.93	−1.89	−1.99/−2.11/−1.96

n.r. not resolved.

From Figure 4 and Table 1 it can be seen, that the *fac*-[(Mn(CO)$_3$(κ^2-S$_2$NC$_7$H$_4$)(κ^1-PPh$_2$Py))] complex **2** shows less negative reduction potentials and is thus easier to reduce than **1**. We assign this to the available sulfur d-orbitals that contribute to the stabilization of a partial negative charge distribution over the equatorial ligand. The multi-electron redox reactions show a negative potential difference (**1/1**$^-$ vs. **1/1**$^{2-}$ and **2/2**$^-$ vs. **2/2**$^{2-}$). This is indicative of structural changes induced by the first redox reaction that facilitate the second redox event (see below).

Introduction of an axial PPh$_2$Py has no major effect on the reduction of complexes **1** and **2**. Experimental and calculated reduction potentials are very close to those of Mn-PPh$_3$ complexes reported earlier (see Table 1). DFT calculations clearly show that the CV peaks correspond to the two-electron reduction and the second one-electron reduction events, respectively. Previous studies on Mn(I) complexes have shown similar redox processes wherein the first reduction has been assigned to a concerted 2e$^-$ reduction event.[34,38,39] The GGA BP86, hybrid PBE0, and meta-GGA r2scan functionals all give consistent results. BP86 and PBE0 are slightly closer to experimental values, however. The first one electron reduction occurs at less negative potentials of ~ −1.83 V which cannot be resolved in the experimental CV spectra (see Figure 4). This corresponds to reported experimental values of −1.65 to −1.85 V in mono-nuclear Mn(CO)$_3$(diimine)$^{+/0}$ complexes.[34]

Structural Changes during Redox Transitions

The first one-electron reduction (E) is a metal-centered Mn(I) to Mn(0) transition which leads to a partial dissociation of the Mn–S bond of the equatorial ligand. The Mn–S distances increase from 2.51 Å in **1** to 3.50 Å in **1**$^-$ and 3.90 Å in **1**$^{2-}$ (for BP86; further results are given in the ESI). This also holds for the transitions **2/2**$^-$ and **2**$^-$**/2**$^{2-}$ from 2.47 Å to 3.25 Å and 3.79 Å (see ESI). This allows a structural interpretation of the more facile two-electron reduction compared to the first one-electron event (see above). The less prominent structural changes during the second one-electron reduction process explain why the two-electron reduction events **1/1**$^{2-}$ and **2/2**$^{2-}$ correspond to the first experimental peaks in CV spectra.[40,41]

Table 2. Electrochemical data for complexes **1**, **2** and related complexes in CH_3CN.

Complexes	E_{pc}^{red}/V	E_{pa}^{ox}/V	E_{cat}/V	i_{cat}/i_p	k_{obs}/s^{-1}	O.P./V	C.E.
1	−1.97, −2.29	0.93, 1.28	−2.48[a]	56.1	610	1.02	0.89–0.72
2	−1.89, −2.04	1.17	−2.58[a]	56.3	615	1.12	0.92–0.72
(N,N)–Mn–PPh_3	−2.06, −2.36	0.53	−1.95[b]	68	890	1.06	0.75–0.47
(S,N)–Mn–PPh_3	−1.93, −2.07	0.69	−1.88[b]	48	445	0.99	0.77–0.39

[a] Acetic acid, [b] TFA. O.P. = overpotential, C.E. = catalytic efficiency. [Correction added on 25 July 2024, after first online publication: Footnotes and column 3 heading were added.]

Catalytic Hydrogen Evolving Activity of Mono-Nuclear Manganese (I) Complexes

Whereas Mn(I)$P(Ph)_3$ complexes required the presence of the strong trifluoroacetic acid (TFA) to give a detectable hydrogen evolution, the pyridine-substituted complexes **1** and **2** showed catalytic activity even in presence of the weaker acetic acid (AcOH) (see Table 2). This is indicative of a more facile protonation (see above). Also, complexes **1** and **2** were not stable in the presence of TFA, as colourless solutions were obtained on addition of ~ 5–6 mM of acid.

Addition of acetic acid led to the appearance of new irreversible reduction waves, which shifted cathodically and displayed an increase in current peak intensity upon increasing the concentration of acetic acid (up to ~ 78 mM acid) (see Figure 5 and Figure S11). The initial reduction peaks (observed in the absence of acid) disappeared for **1**, while for **2** the initial reduction peaks (−1.89, −2.04) are present but with an anodic shift (i.e., Mn^{I}/Mn^{0} redox couple shifted to a more positive potential) and current did not increase on further addition of acid.

The catalytic peaks (E_{cat}) at −2.48 (**1**) and −2.58 V (**2**) indicate that catalysis occurred with a 1.02 (**1**) and 1.12 V (**2**) overpotential (OP) in CH_3CN (see Table 2).[42–44] In the absence of catalyst, in an acetonitrile/AcOH solution, negligible current was observed for proton reduction (−1.0 to −3.0 V) at the glassy carbon electrode (ESI, Figure S12).

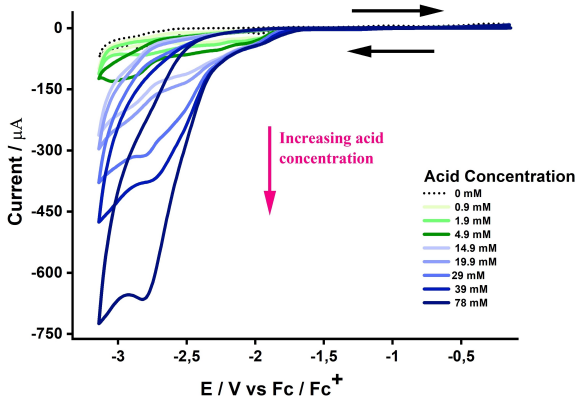

Figure 5. CV spectra for complex **1** (1 mM) in the absence and with increasing concentration of AcOH (0.9–78 mM) at a scan rate of 0.1 Vs^{-1}. CV spectra of complex **2** are given in the ESI.

The structural integrity of the two complexes was confirmed and based upon a comparison of UV-Vis and FTIR spectra measured prior to and after catalysis (ESI, Figure S13). The comparison shows that there is no shift in peak positions and only a minor decrease in peak intensity. The morphology and particle size of the metal complexes (after synthesis) have also been characterized by field emission scanning electron micrography (FESEM) (Figure S14a). In the FESEM of the synthesized Mn complexes, a uniform matrix was noted indicating a homogeneous phase material. FESEM images of the catalysts taken after catalysis of HER in the presence of acid also demonstrate the durability of the catalysts (Figure S14b).

A linear plot for i_{cat}/i_p *vs.* [AcOH] suggests a first-order dependence on the proton concentration (Figure 6a). For the i_{cat} vs. [AcOH] plot see ESI (Figure S15). Both the catalysts were active towards proton reduction with an i_{cat}/i_p ratio (78 mM acid) of 56.1 (**1**) and 56.3 (**2**), corresponding to k_{obs} (s^{-1}) values of 610 (**1**) and 615 (**2**).[44,45] However, the i_{cat}/i_p values represent only an estimate of *TOF* (turn over frequency) as steady-state conditions were still not achieved at this point. As observed from the k_{obs} values, complexes **1** and **2** are comparable catalysts (see Figure 6 **b**). However, complex **1** showed a slightly lower OP than complex **2** with moderate catalytic efficiency. Though the complexes reported in this work showed higher k_{obs} values than the Mn–PPh_3 analogues, a direct comparison cannot be made as different acids were used for electrocatalysis. DFT studies further helped to understand the role of the complexes in proton reduction.

Hydrogen Evolution Reaction Mechanism

Incorporation of either NH or S in the equatorial ligand does not significantly affect the HER mechanism of complexes **1** and **2**. Only BP86 results for the **1** are discussed here in the main text and shown in Figure 7. Results for **2** are almost indistinguishable and can be found in the ESI (Tables S4–S6). Hybrid PBE0 and meta-GGA (r^2SCAN) results are very close and are given in the ESI (Tables S4–S6). Following the first reduction event to give 1^-, the increase in Mn···S distance, in principle,

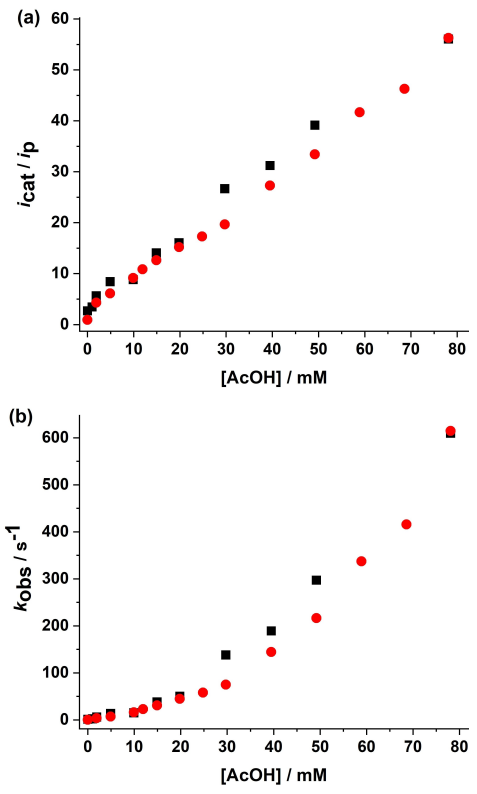

Figure 6. Plots of (a) i_{cat}/i_p vs. [AcOH] and (b) k_{obs}/s^{-1} vs. [AcOH] for complexes (1 mM) **1** (black) and **2** (red) in CH_3CN at 0.1 Vs^{-1}.

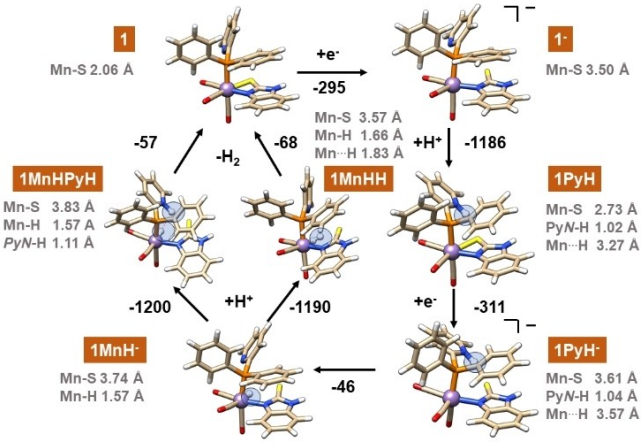

Figure 7. Reaction mechanism of the hydrogen evolution reaction of **1**. Gibbs energies in kJ/mol for each step are given for BP86-D3(BJ)/def2-TZVP (acetonitrile). Results for other functionals are given in the ESI (Tables S8–S12). Alternating electrochemical (E) and protonation (C) steps involve Mn(I)/Mn(0) reduction, protonation of the pyridine nitrogen, an intramolecular proton transfer to form a Mn(I)-hydrido species and a facile release of H_2 from either the Mn•H_2 or MnHPyH complex (see also ESI Schemes S1–S3). More structural details can be found in the ESI, Tables S7–S9.

opens two possible sites for protonation, namely the thiolate or the pyridine nitrogen atom. Figure S16 shows the metal-based reduction event and the unpaired spin density distribution localized at the Mn atoms. However, protonation of the thiolate sulphur atom is less favoured by 22–39 kJ/mol, depending on functional. Protonation of the pyridine nitrogen atom to give **1PyH** leads to a rebinding of the equatorial ligand. Thus, the axial pyridine is enhancing the catalyst's stability. The second one-electron reduction to **1PyH**$^-$ is followed by an intramolecular proton transfer to yield the Mn hydride **1MnH**$^-$. In order to complete the catalytic cycle, the second protonation can be either hydride- (to give **1MnHH**) or pyridine-based (**1MnPyH**), both of which are differing by a mere 10 kJ/mol and appear feasible. Release of H_2 from either intermediate is thermodynamically favorable and recovers complex **1**.

Conclusions

PPh_2Py-substituted Mn(I) complexes (**1** and **2**) are active catalysts towards electrocatalytic proton reduction in CH_3CN with a weak acid as the proton source. Compared to the PPh_3 complexes which required the stronger TFA acid, introduction of a tertiary nitrogen in the second coordination sphere does not significantly affect the redox transitions. However, it offers an additional site for protonation to give a pyridinium cation, which is thermodynamically favored over thiolate protonation. After pyridine ligand protonation, rebinding of the equatorial ligand enhances the stability of these mono-nuclear manganese (I) catalysts. An intramolecular proton transfer gives the formation of a Mn-hydride complex from which H_2 release is either occurring in a metal-centered or ligand-assisted pathway. Such a reaction pathway has not been reported before for mono-nuclear Mn(I) complexes. So far, Mn(I)-hydrido PNP complexes are known to be efficient and selective non-precious CO_2 to methanol reduction catalysts.[31] The introduction of a secondary coordination sphere basic nitrogen atom thus allows a solvent-accessible and facile initial protonation to control the catalysts' reaction performance. A similar effect was already seen for a pyridine ligand in a bi-nuclear FeFe complex where its positioning was controlling the site of HER. Compared to flexible aliphatic amines, the pyridine ligand is free from intra-ligand conformers and thus pre-oriented for an efficient proton transfer to the metal. This is an important aspect in catalyst design that ought to be considered when designing efficient intramolecular proton transfer paths.

Experimental Details

Details of Synthesis

The starting dinuclear {MnMn} complexes **A** and **B** were synthesized according to literature.[37,46–48]

fac-$[(Mn(CO)_3(\kappa^2\text{-}SN_2C_7H_5)(\kappa^1\text{-}PPh_2Py))]$ **1**

A dichloromethane solution (30 ml) of $[Mn_2(CO)_6(\mu\text{-}SN_2C_7H_5)_2]$ **A** (100 mg, 0.17 mmol) and Diphenyl-2-pyridyl phosphine (**L**^{1}) (105.5 mg, 0.34 mmol) was stirred at room temperature for 72 h. The solvent was then removed under reduced pressure and the crude product was chromatographed on a silica gel column. Elution with hexane/dichloromethane (3:2, v/v) resulted in two bands. A faster moving band gave traces of complex **A** whereas the slower

moving band gave a yellow-colored product as complex **1**. Complex **1**: Yield: 67 mg (71%); ^{1}H NMR (400 MHz, $CDCl_3$, ppm): $\delta =$ 6.84–8.71 (18H, aromatic protons, thiol/**L**^{1}), 7.68 (NH proton); ^{31}P NMR (161.8 MHz, $CDCl_3$, ppm): $\delta = 56.5$; FTIR (ν_{CO}, CH_2Cl_2, cm^{-1}): 2021 (br), 1939 (br), 1906 (br); ESI-MS (CH_3CN): *m/z* calcd for $[\mathbf{1}]^+$: 551.03; found: 552.03 $[\mathbf{1}+H]^+$; elemental analysis calcd (%) for $C_{27}H_{19}MnN_3SO_3P$: C 58.81, H 3.47, N 7.62, S 5.81; found: C 58.98, H 3.77, N 7.82, S 5.97.

fac-$[(Mn(CO)_3(\kappa^2\text{-}S_2NC_7H_4)(\kappa^1\text{-}PPh_2Py))]$ **2**

A dichloromethane solution (30 ml) of $[Mn_2(CO)_6(\mu\text{-}S_2NC_7H_4)_2]$ **B** (100 mg, 0.16 mmol) and Diphenyl-2-pyridyl phosphine (**L**^{1}) (84 mg, 0.32 mmol) was stirred at RT for 72 h. The solvent was then removed under reduced pressure and the crude product was chromatographed on a silica gel column. Elution with hexane/dichloromethane (3:2, v/v) resulted in two bands. A faster moving band gave traces of complex **B** whereas the slower moving band gave a yellow-colored product as complex **2**. Complex **2**: Yield: 84 mg (92%); ^{1}H NMR (400 MHz, $CDCl_3$, ppm): $\delta = 7.06$–8.41 (18H, aromatic protons, thiol/**L**^{1}); ^{31}P NMR (161.8 MHz, $CDCl_3$, ppm): $\delta =$ 57.4; FTIR (ν_{CO}, CH_2Cl_2, cm^{-1}): 2022 (br), 1942 (br), 1909 (br); ESI-MS (CH_3CN) *m/z* calcd for $[\mathbf{2}]^+$: 567.98; found: 568.99 $[\mathbf{2}+H]^+$; elemental analysis calcd (%) for $C_{27}H_{18}MnN_2S_2O_3P$: C 57.05, H 3.19, N 4.93, S 11.28; found: C 56.99, H 3.21, N 5.00, S 11.25.

General Methods, Materials, and Instrumentation

All solvents and chemicals were purchased from Sigma Aldrich and were used without further purification. Synthesis of complexes **1** and **2** was carried out according to the procedure described in literature.[35] A JEOL 400 MHz NMR Spectrometer was used to record the ^{1}H and ^{31}P NMR at room temperature in $CDCl_3$ solution. A Perkin Elmer FTIR Spectrometer was used for recording the FTIR spectra from CH_2Cl_2 solutions of the samples over the range 400–4000 cm^{-1}. The UV-Vis spectra for complexes were recorded in CH_3CN on a Perkin-Elmer Lambda spectrophotometer. Mass spectra were recorded with a Quadrupole Time-of-flight mass spectrometer with ESI and APCI source (Agilent G6530AA (LC-HRMS–Q-TOF)). FESEM images were recorded using a Zeiss GeminiSEM 500. Elemental (C, H, and N) analyses were performed on a Leco TruSpec Micro CHNS analyzer.

Electrochemical Measurements

Cyclic voltammetric (CV) measurements were conducted in CH_3CN (under Argon atmosphere) with 0.1 M $[N(n\text{-}Bu_4)][PF_6]$ (tetrabutylammonium hexafluorophosphate) as the supporting electrolyte that was dried in vacuum at 383 K. CV curves for the electrocatalytic activity of **1** and **2** (1 mM) were obtained upon the addition of known concentrations of acetic acid (AcOH) (pK_a in $CH_3CN = 23.51$, E^0 in $CH_3CN = -1.46$ V). An Autolab potentiostat (PGSTAT302 N) with a Nova 1.11 advanced software was used to carry out the cyclic voltammetry measurements. Glassy carbon disc (diameter 3 mm, freshly polished) was chosen as a working electrode for cyclic voltammetry. Platinum wire was used as the counter electrode. The reference electrode was a non-aqueous Ag/Ag^+ electrode (CH Instruments, 0.01 M $AgNO_3$ in CH_3CN). All the potentials are quoted against the ferrocene ferrocenium couple (Fc/Fc^+); ferrocene was added as an internal standard at the end of the experiments. For electrochemical measurements, all solutions were prepared from dry CH_3CN (Sigma-Aldrich, spectroscopic grade, dried with molecular sieves (MS, 3 Å). For bulk electrolysis experiments, a carbon rod was used as the working electrode with platinum as the counter electrode and non-aqueous Ag/Ag^+ as the reference electrode (CH Instruments, 0.01 M $AgNO_3$ in CH_3CN).

X-ray Crystallography

X−ray crystal data for complexes **1** and **2** was collected on a Rigaku (Oxford diffraction) XtaLAB Synergy-S single crystal X−ray diffractometer using Mo–Kα (λ = 0.71073 Å) radiation. Significant crystallographic parameters and refinement details are listed in Tables S1–S3. The structures were solved and refined by full-matrix least-squares techniques on F2 using the SHELX-2018 (SHELXTL program package).[49] The structures were solved and refined by standard procedures. Multi-scan absorption correction was applied. The coordinates of non-hydrogen atoms were refined anisotropically using SHELXL-2018.[50] All calculations were done using the *Wingx* software package..[51] For the molecular graphics, the program OLEX-2 was used.[52]

Computational Details

All calculations were carried out in Turbomole 7.5.1[53,54] with Grimme dispersion corrections.[55,56] Geometry optimization as well as frequency calculations are performed with BP86-D3,[57,58] PBE0-D3[59] and r^{2}SCAN-D4[60] exchange-correlation functionals along with def2-TZVP basis sets.[61] Solvation in acetonitrile solvent (dielectric constant ε = 37.5) was considered using the COSMO solvation model.[62] The redox potentials of all complexes were calculated relative to Fc/Fc^+ reference electrode.

Supporting Information

Deposition Numbers CCDC-2337353 (**1**) and CCDC-2337354 (**2**) for the complexes, contain the supplementary crystallographic data for this paper. These data are provided free of charge by the joint Cambridge Crystallographic Data Centre and Fachinformationszentrum Karlsruhe Access Structures service. The spectroscopic data and Cartesian coordinates of all structures associated with this article are available free of charge in ESI (Electronic Supplementary Information). Additional experimental results, calculated structural parameters as well as energetics are available as Supplementary Information.

Acknowledgements

We thank the Max Planck Society for the Advancement of Science (MPG) to MS and MJ, the Institution of Eminence (IoE), University of Delhi (Faculty Research Programme Grant-IoE, Ref. No./IoE/2023-24/12/FRP to SKG) for financial support. This work is part of the Research Initiative "SmartProSys: Intelligent Process Systems for the Sustainable Production of Chemicals" funded by the Ministry for Science, Energy, Climate Protection and the Environment of the State of Saxony-Anhalt. FAH is grateful to the ICCR (Indian Council for Cultural Relations), University of Bablony, Iraq, and University of Delhi for research scholarships. SKG is thankful to University of Delhi for its instrumentation facilities. Open Access funding enabled and organized by Projekt DEAL.

Conflict of Interests

The authors declare no conflict of interest.

Data Availability Statement

The data that support the findings of this study are available in the supplementary material of this article.

Keywords: hydrogen generation · bioinorganic · proton shuttle · mono-nuclear catalyst · reaction mechanism

[1] S. S. Penner, *Energy* **2006**, *31*, 33–43.
[2] M. A. Rosen, S. Koohi-Fayegh, *Energy, Ecology and Environment* **2016**, *1*, 10–29.
[3] R. Cammack, M. Frey, R. Robson (Eds.), Hydrogen as a Fuel, CRC Press, London, **2001**.
[4] S. Kaur-Ghumaan, L. Schwartz, R. Lomoth, M. Stein, S. Ott, *Angew. Chem. Int. Ed.* **2010**, *49*, 8033–8036.
[5] M. Natarajan, H. Faujdar, S. M. Mobin, M. Stein, S. Kaur-Ghumaan, *Dalton Trans.* **2017**, *46*, 10050–10056.
[6] M. Fang, E. S. Wiedner, W. G. Dougherty, W. S. Kassel, T. Liu, D. L. DuBois, R. M. Bullock, *Organometallics* **2014**, *33*, 5820–5833.
[7] V. Artero, J.-M. Saveant, *Energy Environ. Sci.* **2014**, *7*, 3808–3814.
[8] J. L. Dempsey, B. S. Brunschwig, J. R. Winkler, H. B. Gray, *Acc. Chem. Res.* **2009**, *42*, 1995–2004.
[9] A. D. Wilson, R. H. Newell, M. J. McNevin, J. T. Muckerman, M. Rakowski DuBois, D. L. DuBois, *J. Am. Chem. Soc.* **2006**, *128*, 358–366.
[10] D. Brazzolotto, M. Gennari, N. Queyriaux, T. R. Simmons, J. Pecaut, S. Demeshko, F. Meyer, M. Orio, V. Artero, C. Duboc, *Nat. Chem.* **2016**, *8*, 1054–1060.
[11] M. R. DuBois, D. L. DuBois, *C. R. Chim.* **2008**, *11*, 805–817.
[12] N. Wang, X.-P. Zhang, J. Han, H. Lei, Q. Zhang, H. Zhang, W. Zhang, U.-P. Apfel, R. Cao, *Chin. J. Catal.* **2023**, *45*, 88–94.
[13] X. Peng, J. Han, X. Li, G. Liu, Y. Xu, Y. Peng, S. Nie, W. Li, X. Li, Z. Chen, H. Peng, R. Cao, Y. Fang, *Chem. Commun.* **2023**, *59*, 10777–10780.
[14] X. Peng, M. Zhang, H. Qin, J. Han, Y. Xu, W. Li, X.-P. Zhang, W. Zhang, U.-P. Apfel, R. Cao, *Angew. Chem. Int. Ed.* **2024**, *63*, e202401074.
[15] A. Silakov, B. Wenk, E. Reijerse, W. Lubitz, *Phys. Chem. Chem. Phys.* **2009**, *11*, 6592–6599.
[16] Ö. F. Erdem, M. Stein, S. Kaur-Ghumaan, E. J. Reijerse, S. Ott, W. Lubitz, *Chem. - Eur. J.* **2013**, *19*, 14566–14572.
[17] S. Raugei, S. Chen, M.-H. Ho, B. Ginovska-Pangovska, R. J. Rousseau, M. Dupuis, D. L. DuBois, R. M. Bullock, *Chem. - Eur. J.* **2012**, *18*, 6493–6506.
[18] A. A. Salamatian, K. L. Bren, *FEBS Lett.* **2023**, *597*, 174–190.
[19] J. M. Le, K. L. Bren, *ACS Energy Lett.* **2019**, *4*, 2168–2180.
[20] S. Lin, S. Banerjee, M. T. Fortunato, C. Xue, J. Huang, A. Y. Sokolov, C. Turro, *J. Am. Chem. Soc.* **2022**, *144*, 20267–20277.
[21] D. Majumder, S. Kolay, V. S. Tripathi, *Electrocatalysis* **2023**, *14*, 602–610.
[22] B. Reuillard, C. Costentin, V. Artero, *Angew. Chem. Int. Ed.* **2023**, *62*, e202302779.
[23] A. Orthaber, M. Karnahl, S. Tschierlei, D. Streich, M. Stein, S. Ott, *Dalton Trans.* **2014**, *43*, 4537–4549.
[24] I. K. Pandey, T. Agarwal, S. M. Mobin, M. Stein, S. Kaur-Ghumaan, *ACS Omega* **2021**, *6*, 4192–4203.
[25] G. M. Jacobsen, J. Y. Yang, B. Twamley, A. D. Wilson, R. M. Bullock, M. Rakowski DuBois, D. L. DuBois, *Energy Environ. Sci.* **2008**, *1*, 167–174.
[26] N. Queyriaux, D. Sun, J. Fize, J. Pécaut, M. J. Field, M. Chavarot-Kerlidou, V. Artero, *J. Am. Chem. Soc.* **2020**, *142*, 274–282.
[27] I. K. Pandey, T. Agarwal, S. M. Mobin, M. Stein, S. Kaur-Ghumaan, *ACS Omega* **2021**, *6*, 4192–4203.
[28] G. R. F. Orton, S. Belazregue, J. K. Cockcroft, F. Hartl, G. Hogarth, *J. Organomet. Chem.* **2023**, *991*, 122673.
[29] S. Ezzaher, J.-F. Capon, F. Gloaguen, F. Y. Pétillon, P. Schollhammer, J. Talarmin, N. Kervarec, *Inorg. Chem.* **2009**, *48*, 2–4.
[30] M. Hirahara, A. Shoji, M. Yagi, *Eur. J. Inorg. Chem.* **2014**, *2014*, 595–606.
[31] F. Bertini, M. Glatz, B. Stöger, M. Peruzzini, L. F. Veiros, K. Kirchner, L. Gonsalvi, *ACS Catal.* **2019**, *9*, 632–639.
[32] F. Bertini, M. Glatz, N. Gorgas, B. Stöger, M. Peruzzini, L. F. Veiros, K. Kirchner, L. Gonsalvi, *Chem. Sci.* **2017**, *8*, 5024–5029.
[33] V. Kaim, S. Kaur-Ghumaan, *Eur. J. Inorg. Chem.* **2019**, *2019*, 5041–5051.
[34] W. L. J. Loke, W. Guo, M. Sohail, A. A. Bengali, W. Y. Fan, *Inorg. Chem.* **2022**, *61*, 20699–20708.
[35] V. Kaim, M. Natarajan, S. Kaur-Ghumaan, *ChemistrySelect* **2019**, *4*, 1789–1794.
[36] V. Kaim, M. Joshi, M. Stein, S. Kaur-Ghumaan, *Front. Chem.* **2022**, *10*, 993085.
[37] T. S. M. Abedin, M. R. Moni, S. Ghosh, D. A. Tocher, G. M. G. Hossain, S. M. Mobin, S. E. Kabir, *Polyhedron* **2018**, *152*, 164–171.
[38] M. H. Rønne, M. R. Madsen, T. Skrydstrup, S. U. Pedersen, K. Daasbjerg, *ChemElectroChem* **2021**, *8*, 2108–2114.
[39] M. H. Rønne, D. Cho, M. R. Madsen, J. B. Jakobsen, S. Eom, É. Escoudé, H. C. D. Hammershøj, D. U. Nielsen, S. U. Pedersen, M.-H. Baik, T. Skrydstrup, K. Daasbjerg, *J. Am. Chem. Soc.* **2020**, *142*, 4265–4275.
[40] M. Bourrez, F. Molton, S. Chardon-Noblat, A. Deronzier, *Angew. Chem. Int. Ed.* **2011**, *50*, 9903–9906.
[41] M. D. Sampson, A. D. Nguyen, K. A. Grice, C. E. Moore, A. L. Rheingold, C. P. Kubiak, *J. Am. Chem. Soc.* **2014**, *136*, 5460–5471.
[42] G. A. N. Felton, R. S. Glass, D. L. Lichtenberger, D. H. Evans, *Inorg. Chem.* **2006**, *45*, 9181–9184.
[43] G. A. N. Felton, C. A. Mebi, B. J. Petro, A. K. Vannucci, D. H. Evans, R. S. Glass, D. L. Lichtenberger, *J. Organomet. Chem.* **2009**, *694*, 2681–2699.
[44] M. L. Helm, M. P. Stewart, R. M. Bullock, M. R. DuBois, D. L. DuBois, *Science* **2011**, *333*, 863–866.
[45] E. S. Rountree, B. D. McCarthy, T. T. Eisenhart, J. L. Dempsey, *Inorg. Chem.* **2014**, *53*, 9983–10002.
[46] S. Ghosh, M. S. Alam Mia, E. Begum, G. M. G. Hossain, S. E. Kabir, *Inorg. Chim. Acta* **2012**, *384*, 76–82.
[47] M. A. Hoque, M. A. Miah, M. N. Abser, A. K. Azad, K. N. Khan, M. M. Karim, *J. Bangladesh Chem. Soc.* **2012**, *25*, 62–70.
[48] M. A. Hoque, M. A. Miah, M. N. Abser, A. K. Azad, K. N. Khan, M. M. Karim, *J. Bangladesh Chem. Soc.* **2012**, *25*, 62–70.
[49] G. M. Sheldrick, *SHELX-97: Programs for crystal structure solution and refinement*. University of Göttingen, Göttingen, Germany **1997**
[50] G. M. Sheldrick, *Acta Crystallogr. Sect. A* **2008**, *64*, 112–122.
[51] G. M. Sheldrick, *Acta Crystallogr. Sect. A* **1990**, *46*, 467–473.
[52] O. V. Dolomanov, L. J. Bourhis, R. J. Gildea, J. A. K. Howard, H. Puschmann, *J. Appl. Crystallogr.* **2009**, *42*, 339–341.
[53] Y. J. Franzke, C. Holzer, J. H. Andersen, T. Begusic, F. Bruder, S. Coriani, F. Della Sala, E. Fabiano, D. A. Fedotov, S. Fuerst, S. Gillhuber, R. Grotjahn, M. Kaupp, M. Kehry, M. Krstic, F. Mack, S. Majumdar, B. D. Nguyen, S. M. Parker, F. Pauly, A. Pausch, E. Perlt, G. S. Phun, A. Rajabi, D. Rappoport, B. Samal, T. Schrader, M. Sharma, E. Tapavicza, R. S. Tress, V. Voora, A. Wodynski, J. M. Yu, B. Zerulla, F. Furche, C. Haettig, M. Sierka, D. P. Tew, F. Weigend, *J. Chem. Theory Comput.* **2023**, *19*, 6859–6890.
[54] F. Furche, R. Ahlrichs, C. Haettig, W. Klopper, M. Sierka, F. Weigend, *Wiley Interdiscip. Rev.: Comput. Mol. Sci.* **2014**, *4*, 91–100.
[55] S. Grimme, J. Antony, S. Ehrlich, H. Krieg, *J. Chem. Phys.* **2010**, *132*, 154104/154101.
[56] E. Caldeweyher, S. Ehlert, A. Hansen, H. Neugebauer, S. Spicher, C. Bannwarth, S. Grimme, *J. Chem. Phys.* **2019**, *150*, 154122.
[57] J. P. Perdew, *Phys Rev B Condens Matter* **1986**, *33*, 8822–8824.
[58] A. D. Becke, *Phys. Rev. A* **1988**, *38*, 3098.
[59] C. Adamo, V. Barone, *J. Chem. Phys.* **1999**, *110*, 6158–6170.
[60] S. Ehlert, U. Huniar, J. Ning, J. W. Furness, J. Sun, A. D. Kaplan, J. P. Perdew, J. G. Brandenburg, *J. Chem. Phys.* **2021**, *154*, 061101.
[61] F. Weigend, R. Ahlrichs, *Phys. Chem. Chem. Phys.* **2005**, *7*, 3297–3305.
[62] A. Schäfer, A. Klamt, D. Sattel, J. C. W. Lohrenz, F. Eckert, *Phys. Chem. Chem. Phys.* **2000**, *2*, 2187–2193.

Manuscript received: March 6, 2024
Revised manuscript received: May 27, 2024
Accepted manuscript online: May 28, 2024
Version of record online: July 8, 2024